Original Paper

# Production performance of a post-fracturing elastoplastic model for deep shale gas reservoirs

Dong-Yan Fan [a,b], Can Yang [c], Hai Sun [a,b,*], Jun Yao [a,b], Xia Yan [a,b], Lei Zhang [a,b], Cun-Qi Jia [d], Gloire Imani [b], Si-Cen Lai [b], Liang Zhou [b]

[a] State Key Laboratory of Deep Oil and Gas, China University of Petroleum (East China), Qingdao, 266580, Shandong, China
[b]

(stimulated reservoir volume, SRV) (Bai et al., 2023). However, hydraulic fracturing in deep reservoirs under high temperature and high pressure can also cause extensive plastic deformation in the SRV area (Guo et al., 2020; Liu and Elsworth, 1999; Wang, 2020; Yao et al., 2018; Zhu et al., 2023). Many studies only consider stress changes based on linear elasticity theory, neglecting the impact of plastic deformation on the reservoir (Cao et al., 2016a; Hu et al., 2022; Liang et al., 2024; Shang et al., 2022; Shentu et al., 2024; Zhu et al., 2022). This method simplifies the stress field calculation but often overlooks dynamic changes in permeability and porosity due to plastic deformation. These changes directly affect production, so the impact of plastic deformation in deep reservoirs should not be underestimated (Karim et al., 2022; Kozhevnikov et al., 2024). Ran and Gu (1997) developed a 3D elastoplastic reservoir model, showing significant deviations in predicted pore pressure and effective stress when treating elastoplastic reservoirs as purely elastic. Some studies introduce elastoplastic constitutive equations to describe stress changes in deep shale gas reservoirs (Hu et al., 2019; Liao et al., 2024; Qi et al., 2021; Xing et al., 2020; Zeng et al., 2019) to study hydraulic fracturing effects. Yao et al. (2018) established a mathematical model for elastoplastic hydraulic fracture propagation based on the Drucker–Prager yield criterion and associated flow rules. Liao et al. (2024) developed a 3D finite element model for vertical hydraulic fracture propagation in deep shale reservoirs, using the Drucker–Prager elastoplastic model to analyze the impact of parameters like in situ stress on fracture morphology. Yi et al. (2025) proposed a dynamic fluid–solid coupled mixed-mode fatigue elastoplastic phase field model for simulating crack initiation and propagation in elastoplastic rocks under cyclic fluid loading. Most numerical simulations focus on crack propagation during hydraulic fracturing, with few studies linking hydraulic fracturing-induced plastic deformation to production processes to study the impact on post-fracturing production.

In fluid seepage processes, a continuous flow model is used to describe multiscale flow processes. Increasing gas production causes continuous shale deformation, causing changes in porosity and micro fractures, thereby resulting in the formation of different gas transport mechanisms such as gas slippage, Knudsen and surface diffusion. These transport mechanisms are linearly superimposed or weighted to obtain an apparent model of multiscale gas flow in shale. Javadpour (2009) proposed an apparent model for gas flow in shale reservoirs based on the linear superposition of surface diffusion and Knudsen diffusion. Li (2012) suggested that gas transport mechanisms in shale nanopores mainly involve continuous flow and Knudsen diffusion, superimposing these mechanisms according to their contributions. Wu et al. (2016) combined slip flow and Knudsen diffusion mechanisms according to their relative contributions to establish a comprehensive model considering surface diffusion and real gas effects. Zhang et al. (2018) derived expressions for the porosity sensitivity exponent and pore compressibility based on a dual porosity model, aiming to clarify the relationship between the stress sensitivity and pore structure of shale. In studying multiscale flow mechanisms of shale gas, many researchers propose coupling flow mechanisms with geomechanics and establishing mathematical models for porosity and permeability variations with effective stress based on the coupled theory proposed by Terzaghi (1943) and the more comprehensive consolidation theory further developed by Biot (1941, 1955). Jiang and Yang (2018) proposed a fully coupled model of fluid flow and geomechanics to simulate complex production phenomena in fractured shale gas reservoirs. Wei et al. (2021) proposed a discontinuous discrete fracture model for the coupling of seepage and geomechanics in fractured reservoirs based on the finite element method. It can be used to simulate the hydraulic fracturing of horizontal wells and the production process of shale oil reservoirs. Li and Liu (2023) established a general permeability model considering effective stress, gas adsorption, and flow regime effects. However, existing studies typically focus either on fracture propagation or couple flow with linear elastic geomechanics, often neglecting the impact of post-fracturing plastic deformation on long-term production. Although some models have incorporated elastoplastic behavior during fracture initiation, few have dynamically linked post-fracturing elastoplastic deformation with evolving multiscale gas flow mechanisms throughout the production stage. Moreover, current multiscale flow models rarely reflect the feedback loop between stress redistribution and flow parameters such as permeability and porosity in a plastic-deforming reservoir.

In this work, we address these gaps by developing a fully coupled elastoplastic flow-geomechanics model that dynamically captures stress-dependent variations in porosity and permeability under multiscale transport regimes. Unlike previous models, our approach integrates elastoplastic stress evolution with surface diffusion, slip flow, and Knudsen diffusion throughout the gas production lifecycle, providing a more realistic and accurate framework for deep shale reservoir performance evaluation.

The organization of this paper is as follows. Section 2 introduces the mathematical model considering post-fracturing plastic deformation. Section 3 introduces model validation and practical applications. Section 4 presents the results and discussion. The conclusion is in Section 5.

## 2. Model development

Our main objective is to develop the model of fractured horizontal well with post-fracturing elastoplastic deformation in deep shale gas reservoirs. In this section, a physical model and governing equations for shale deformation and gas flow are established, and dynamic coupling methods are discussed.

### 2.1. Physical model

Shale reservoirs have nanopores and natural fracture systems crucial for gas storage. Due to significant size differences in these features, gas migration involves complex multiphase mechanisms, including adsorption–desorption, Knudsen diffusion, surface diffusion, and gas slip. As illustrated in Fig. 1, gas molecules adsorb onto the shale matrix to form adsorbed gas and desorb into free gas when the reservoir conditions change. Simultaneously, free gas moves through Knudsen diffusion within the matrix towards natural fractures along the concentration gradient. Surface diffusion aids gas movement on the shale surface, facilitating overall migration. Gas near natural fractures then penetrates and accelerates transport via gas slippage. Finally, gas enters hydraulic fractures and is produced through horizontal wells.

The deformation of shale formations during extraction is shown in Fig. 2. During fracturing, continuous loading causes extensive plastic deformation around hydraulic fracture tips. During production, the continuous decline in gas pressure alters the effective stress field. The volume changes of shale due to gas adsorption and desorption are also considered. Deformation resulting from both production and fracturing ultimately leads to dynamic variation in reservoir permeability.

Clearly, deep shale gas development involves multi-physical processes. Cross-coupled equations dynamically link reservoir deformation and fluid seepage, illustrating system couplings as shown in Fig. 3. This paper will use a set of partial differential equations to derive mathematical models for each physical process, studying the coupling relationships between physical fields.

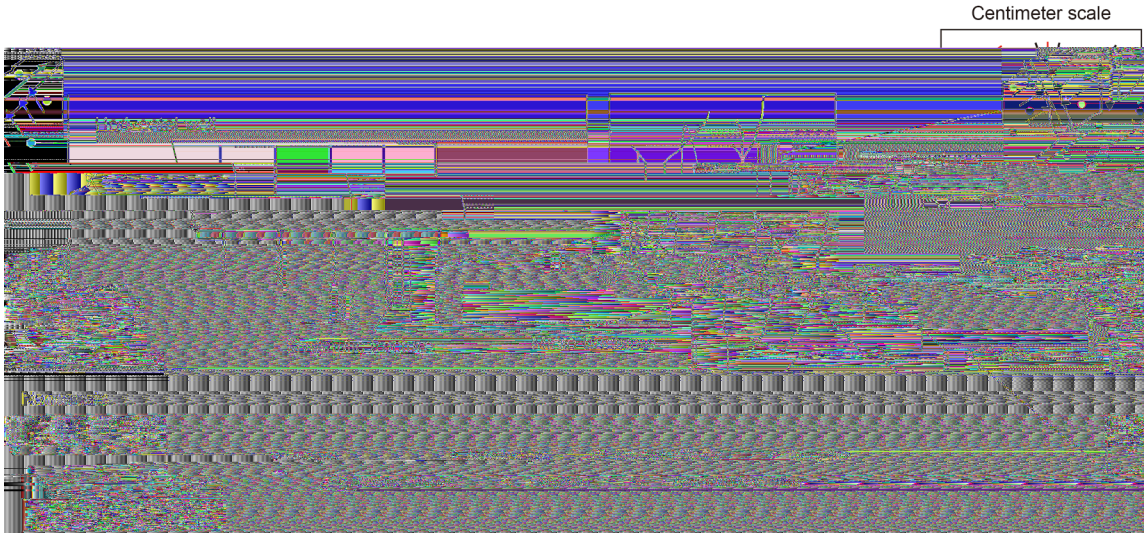


**Fig. 1.** Schematic diagram of multi-scale gas migration mechanisms in shale.

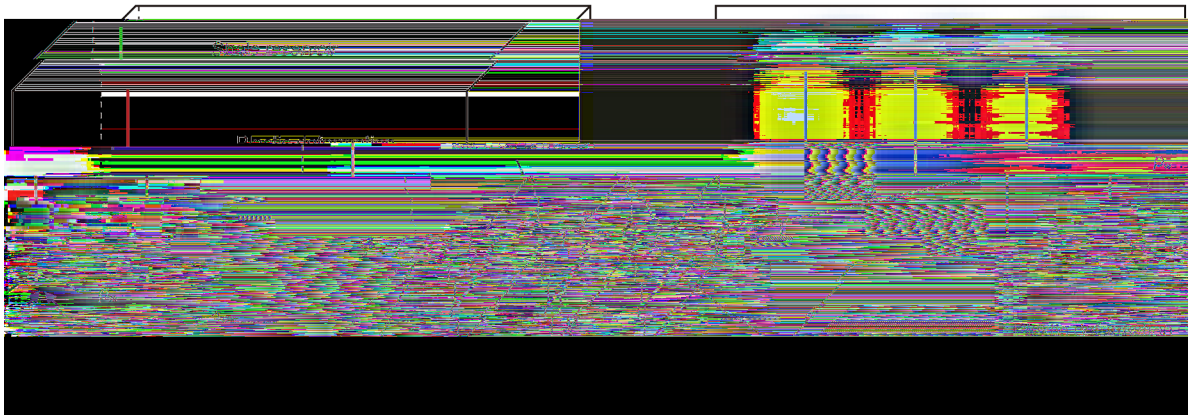

**Fig. 2.** Plastic deformation in shale reservoir.

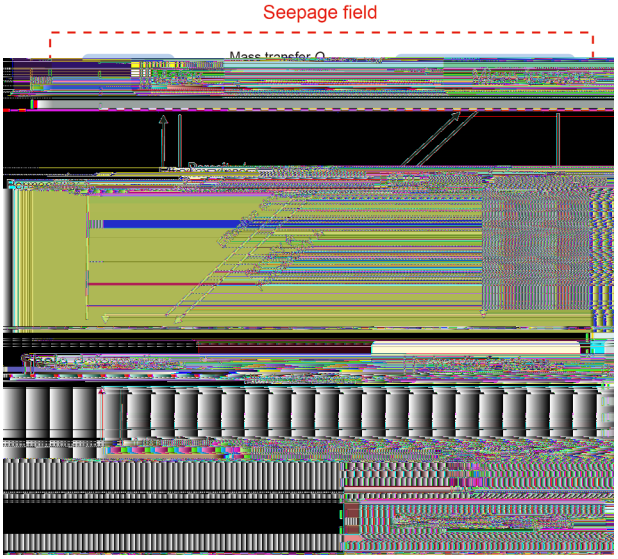


**Fig. 3.** Coupling relationships of multi-physical processes among different systems.

### 2.2. Governing equation of shale deformation

This section focuses on the plastic characteristics of shale rock. Combining the elastoplastic properties of the formation after fracturing and the elastic properties during production, a comprehensive elastoplastic model for deep shale gas hydraulic fracturing in horizontal wells is established.

#### 2.2.1. Elastic model for production processes

The stress field during production is described as elastic deformation. Considering the effect of pore fluid pressure on shale deformation, based on Biot's consolidation theory (Biot, 1955) and adsorption strain (Zhang et al., 2008), the constitutive equations for the matrix and natural fractures are as follows:

$$\begin{aligned}\boldsymbol{\sigma}_{ij} &= 2G_{\mathrm{m}}\varepsilon_{ij} + 2G_{\mathrm{m}}\frac{\nu_{\mathrm{m}}}{1-\nu_{\mathrm{m}}}\varepsilon_{\mathrm{kk}} - \alpha p_{\mathrm{m}}\delta_{ij} - K_{\mathrm{m}}\varepsilon_{\mathrm{s}}\delta_{ij} \\ \boldsymbol{\sigma}_{ij} &= 2G_{\mathrm{f}}\varepsilon_{ij} + 2G_{\mathrm{f}}\frac{\nu_{\mathrm{f}}}{1-\nu_{\mathrm{f}}}\varepsilon_{\mathrm{kk}} - \beta p_{\mathrm{f}}\delta_{ij}\end{aligned} \tag{1}$$

with $G = E/2(1+\nu)$, where subscripts m and f represent the shale matrix and natural fractures, respectively; $G$ is the shear modulus, Pa; $\nu$ is Poisson's ratio; $E$ is the Young's modulus, Pa; $p$ is pressure, Pa; $\alpha$ is the Biot coefficient of matrix; $\beta$ is the Biot coefficient of

natural fractures; $\varepsilon_{kk}$ is the volume strain; $\varepsilon_s$ is the adsorbed volume strain of shale matrix. The adsorption-induced volume strain is described by the modified Langmuir-type equation (Langmuir, 1968; Mehrabian and Abousleiman, 2015; Pan and Connell, 2012; Tuncay and Corapcioglu, 1995): $\varepsilon_s = \varepsilon_L p_m/(p_L + p_m)$. $\varepsilon_L$ is the maximum adsorptive volume strain of the matrix; $p_L$ is the

density, kg/m$^3$; $V_L$ is the Langmuir volume constant, m$^3$/kg; $S_{gm}$ is the gas saturation in the matrix; $S_{wm}$ is the water saturation in the matrix; $S_{gf}$ is the gas saturation in the natural fractures; $S_{wf}$ is the water saturation in the natural fractures.

The gas–water exchange term between the natural fractures and the matrix is given by

$$\begin{cases} Q_{gmf} = \rho_{gm} M_g k_m \alpha_g \left(p_{gm} - p_{gf}\right) \Big/ \left(RT_s Z_m \mu_g\right) \\ Q_{wmf} = \rho_{wm} k_m \alpha_w \left(p_{wm} - p_{wf}\right) \Big/ \mu_w \end{cases} \tag{6}$$

where $R$ is the universal gas constant, J/(mol□K); $M_g$ is the molar mass of the gas, kg/mol; $a_g$ and $a_w$ respectively represent inter-porosity flow coefficients of gas and water; $Z_m$ is the $Z$ factor in the matrix system; $T_s$ is the temperature of initial condition.

The formula for shale matrix permeability, considering simultaneously Knudsen diffusion, surface diffusion, adsorption–desorption, gas slip, and stress sensitivity, can be expressed as follows:

$$k_{m1} = \frac{1+F}{m} k_{m0} \left[ \left(1 + \frac{\mu_m D_{km}}{p_m k_{m0}}\right) + k_{sf} \right] \tag{7}$$

where $k_{m0}$ is the initial matrix permeability, m$^2$; $k_{sf}$ is the apparent permeability of the shale matrix characterized by surface diffusion, m$^2$; $D_{km}$ is the diffusion coefficient in the matrix; $F$ is the slippage correction factor; $m$ is the stress sensitivity coefficient.

### 2.4. Dynamic coupling equations

A dynamic coupling model considering post-fracturing rock plastic deformation and multi-scale transport mechanisms is established by dynamically coupling effective stress with permeability and porosity.

#### 2.4.1. Dynamic porosity and permeability of matrix

According to previous studies (Cao et al., 2016b; Wang et al., 2018), the dynamic porosity model for the matrix can be expressed as follows:

$$\phi_m = \frac{(1+M_0)\phi_{m0} + \alpha(M - M_0)}{1+M} \tag{8}$$

with

$$M = \varepsilon_{kk} + \frac{\left(S_{gm} p_{gm} + S_{wm} p_{wm}\right)}{K_s} - \varepsilon_s$$

$$M_0 = \varepsilon_{kk0} + \frac{\left(S_{gm0} p_{gm0} + S_{wm0} p_{wm0}\right)}{K_s} - \varepsilon_{s0}$$

$$\varepsilon_{kk} = \frac{\overline{\sigma_m}}{K_m} + \varepsilon_s$$

$$\overline{\sigma_m} = \frac{1}{3}\sigma_{kk} + \alpha\left(S_{gm} p_{gm} + S_{wm} p_{wm}\right)$$

$$\sigma_{kk} = \left(\sigma_\theta^p + \sigma_r^p + \sigma_c\right)/3$$

where $\varepsilon_{s0}$ is the initial adsorption strain; $\varepsilon_{kk0}$ is the initial volume strain of the shale; $\varepsilon_{kk}$ is the volume strain of shale; $\overline{\sigma_m}$ is the effective stress within the matrix; $\sigma_{kk}$ is the volume stress; $\sigma_\theta^p$ is the tangential stress (plastic); $\sigma_r^p$ is the radial stress (plastic).

Based on the numerous permeability models, the Kozeny–Carman equation is the most widely used permeability model (Xu and Yu, 2008). The coupled permeability of shale matrix, considering Knudsen diffusion, surface diffusion, adsorption–desorption, gas slip, stress sensitivity, and rock elastoplastic deformation, can be expressed as follows:

$$k_m = \frac{1+F}{m} k_{m0} \left[ \left(1 + \frac{\mu_m D_{km}}{p_m k_{m0}}\right) + k_{sf} \right] \left(\frac{\phi_m}{\phi_{m0}}\right)^3 \tag{9}$$

#### 2.4.2. Dynamic porosity and permeability of natural fracture

Compression and matrix deformation cause changes in the aperture of natural fractures, thereby altering the porosity and original permeability of the natural fractures. According to scholars' research, the porosity model for natural fractures can be expressed as follows (Zhao et al., 2020):

$$\phi_f = \phi_{f0} \exp\left[ \frac{\overline{\sigma_f} - \overline{\sigma_{f0}}}{K_p} - \frac{\overline{\sigma_m} - \overline{\sigma_{m0}}}{K_m} - (\varepsilon_s - \varepsilon_{s0}) \right] \tag{10}$$

with

$$\overline{\sigma_f} = \frac{1}{3}\sigma_{kk} + \beta\left(S_{gf} p_{gf} + S_{wf} p_{wf}\right)$$

where $\overline{\sigma_{f0}}$ is the initial effective stress in natural fractures; $\overline{\sigma_{m0}}$ is the initial effective stress in the matrix; $\overline{\sigma_f}$ is the effective stress within the natural fracture. According to the cubic relationship between natural fracture porosity and permeability (Wu et al., 2011), the dynamic permeability model for natural fractures is

$$k_f = k_{f0} \frac{1+F}{m} \exp\left\{ 3\left[ \frac{\overline{\sigma_f} - \overline{\sigma_{f0}}}{K_p} - \frac{\overline{\sigma_m} - \overline{\sigma_{m0}}}{K_m} - (\varepsilon_s - \varepsilon_{s0}) \right] \right\} \tag{11}$$

where $k_{f0}$ is the initial permeability of shale natural fractures.

The above dynamic coupling equations between shale deformation and gas flow, combined with the governing equations of plastic deformation and gas flow, form a fully coupled multi-physics model.

## 3. Model implementation and validation

In this section, the finite element method will be used to solve the established coupled flow and geomechanics model. The accuracy of the model will be verified by the classic mechanical Mandel problem (Mandel, 1953) and practical applications.

### 3.1. Model validation

The physical model is a rectangular porous elastic medium filled with fluid, sandwiched between two frictionless rigid plates.

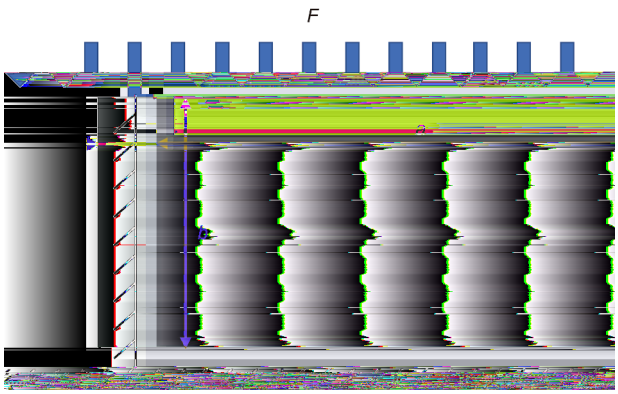


**Fig. 4.** Schematic diagram of the Mandel problem model.

The sides are drained with no traction and an instantaneous force acts on the top surface. The geometric model of the Mandel problem is shown in Fig. 4. A numerical model is constructed using parameters in Table 1. Due to symmetry in structure and loading, only a quarter of the domain is generated. Goulet et al. (2009) provided the analytical solution for pore pressure. The calculated pore pressure on the top interface is compared with the analytical solution in Fig. 5, showing good agreement and confirming the model's accuracy.

### 3.2. Practical applications

Well Y1 is a deep shale gas well in the Sichuan Basin at a depth of 3845 m. The porosity ranges from 2.1% to 9.6%, averaging 5.5%. The matrix porosity averages between 4.6% and 5.4%. Permeability ranges from 0.01 to 0.20 mD, averaging 0.06 mD. Gas content ranges from 3.3 to 8.5 $m^3$/t, averaging 5.5 $m^3$/t. Table 2 shows the reservoir and fracturing parameters.

Based on the daily and cumulative gas production curves of Well Y1 (Figs. 6 and 7), the model's fit closely matches the actual production dynamics during normal operation. The high overall fitting accuracy indicates good model performance. Compared to the elastic model, the elastoplastic model aligns with the actual production of Well Y1, demonstrating its applicability to real production wells.

## 4. Results and discussion

In this section, the impact of the elastoplastic model on the permeability of the matrix and natural fractures is compared in deep shale gas reservoirs. Then, the effects of various parameters are discussed on production, then the principal factors are obtained.

**Table 1**
Calculation parameters for the Mandel problem.

| Parameter | Value |
|---|---|
| Biot coefficient | 0.93 |
| Poisson's ratio | 0.2 |
| Young's modulus, GPa | 15 |
| Fluid compressibility modulus, MPa | 3000 |
| Porosity | 0.1 |
| Permeability, mD | 100 |

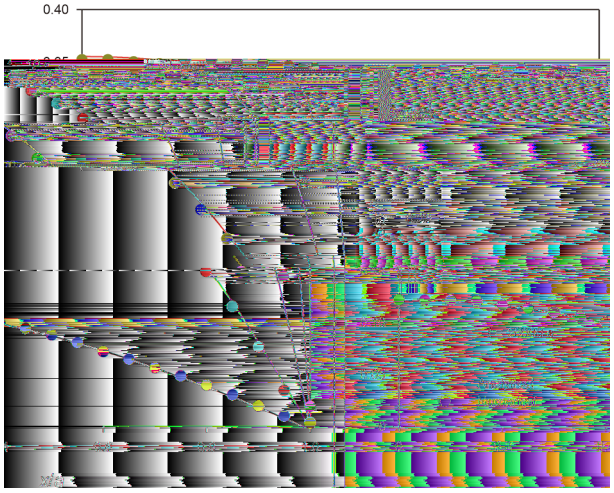


**Fig. 5.** Comparison of numerical simulation results with analytical solution.

### 4.1. Model implementation

This section is to establish a dynamic numerical model simulating the production of deep hydraulically fractured horizontal wells considering shale elastoplastic deformation. The model is symmetric around the wellbore. The geometry of the two-dimensional model is illustrated in Fig. 8. The dimensions of the model are 500 m horizontally and 150 m vertically. The total length of the horizontal well is 400 m with a half-fracture length of 90 m. There are four hydraulic fractures, spaced 100 m apart. The reservoir is initially at a uniform pressure, the model is subjected to an initial pore pressure of 50 MPa, with constant pressure production at a flowing bottom-hole pressure of 30 MPa. The left, right, and top boundaries are mechanically constrained with zero normal displacement, representing impermeable and rigid boundaries. The entire model is treated as elastoplastic material. Material properties for the baseline case are listed in Table 3. The relative permeability curves of the matrix and natural fractures are

**Table 2**
Basic reservoir parameters.

| Parameter | Value | Parameter | Value |
|---|---|---|---|
| Reservoir pressure, MPa | 90 | Gas density, kg/$m^3$ | 0.4 |
| Formation temperature, K | 408.15 | Gas molar mass, kg/mol | 0.0195 |
| Fracture length, m | 80 | Fracture width, m | 0.003 |
| Horizontal well length, m | 1500 | Horizontal well spacing, m | 300 |
| Number of fracture stages | 20 | BHP, MPa | 20 |
| Reservoir thickness, m | 37 | Wellbore radius, m | 0.1 |
| Matrix porosity, % | 5.5 | Depth, m | 3845 |

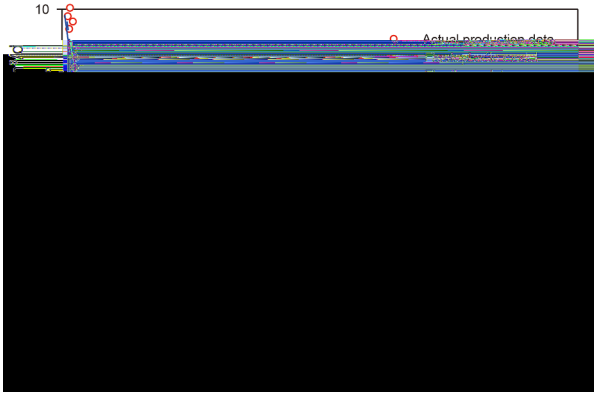


**Fig. 6.** Comparison of model results against the daily production history.

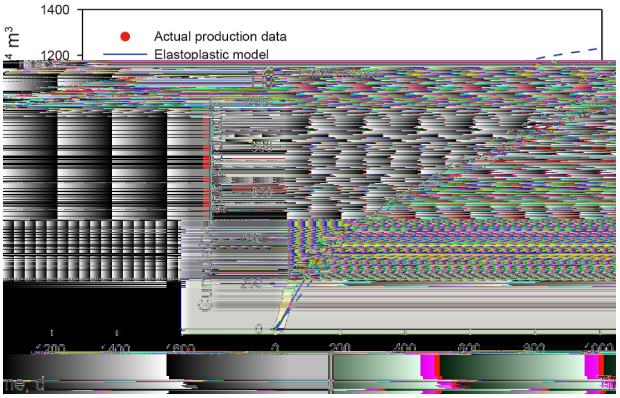


**Fig. 7.** Comparison of model results against the cumulative production history.

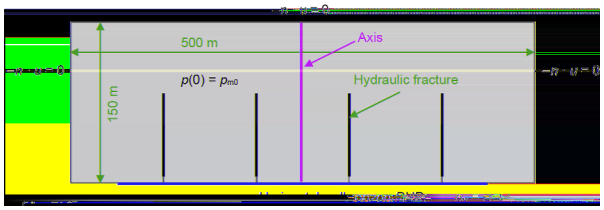


**Fig. 8.** Numerical model considering elastoplastic deformation.

elastic formations increases with distance and decreases with time, while in the elastoplastic formations, the $k_m/k_0$ decreases and then increases with distance, and decreases with time. The minimum $k_m/k_0$ value shifts 25 m outward from 100 to 1000 d. The permeability ratio in elastic formations is always higher than in plastic formations. Fig. 13 shows that the microfracuture permeability has a similar pattern, but the minimum $k_f/k_0$ value shifting 10 m from 300 to 1000 d.

Due to the plasticity of the formation, its permeability is

**Table 3**
Input parameters for basic simulation analysis.

| Parameter | Value | Parameter | Value |
|---|---|---|---|
| Initial matrix porosity $\phi_{m0}$ | 0.00935 | Initial fracture porosity $\phi_{f0}$ | 0.0624 |
| Initial matrix permeability $k_{m0}$, mD | 0.00002 | Stress sensitivity $m$ | 0.1 |
| Slip correction coefficient $F$ | 1.017 | Initial temperature $T_s$, K | 485 |
| Langmuir volume constant $V_L$, $m^3$/kg | 0.00272 | Langmuir pressure $p_L$, MPa | 4.48 |
| Critical pressure $p_c$, MPa | 4.64 | Critical temperature $T_c$, K | 191.05 |
| Initial pressure $p_{m0}$, MPa | 50 | BHP $p_w$, MPa | 30 |
| Gas constant $R$, J/(mol·K) | 8.314 | Gas molar mass $M_g$, kg/mol | 0.016 |
| Natural fracture aperture $b$, mm | 0.009 | Natural fracture spacing s, m | 0.5 |
| Hydraulic fracture aperture $d_f$, m | 0.005 | Rock density $\rho_m$, kg/$m^3$ | 2600 |
| Water viscosity $\mu_w$, mPa·s | 1.0 | Water density $\rho_w$, kg/$m^3$ | 1000 |
| Initial water saturation in the matrix $S_{wm}$ | 0.25 | Initial water saturation in the fracture $S_{wf}$ | 0.55 |
| Young's modulus $E$, GPa | 1.3 | Poisson's ratio $v$ | 0.15 |
| Rock strength $\sigma_c$, MPa | 15 | Langmuir strain constant $\varepsilon_L$ | 0.02295 |

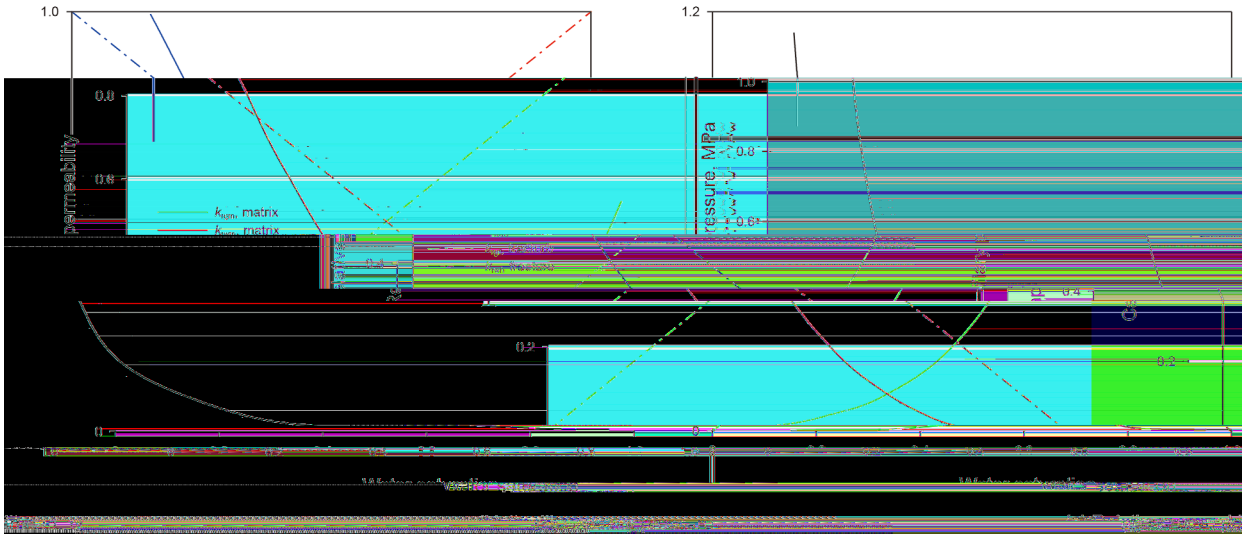


**Fig. 9.** Curves of relative permeability and capillary pressure.

shown in Fig. 9(a), and the capillary pressure curve of the matrix is shown in Fig. 9(b).

### 4.2. Comparison of elastic and elastoplastic models

The matrix and natural fracture permeability plot with BHP of 25 MPa are shown in Figs. 10 and 11. As shale gas is continuously developed, reservoir pressure gradually decreases. This causes pore and natural fracture closure in the near-well zone, reducing matrix and natural fracture permeability, while the matrix and natural fracture permeability of the elastic formation is higher than that of the elastoplastic formation at 25 MPa.

The matrix and natural fracture permeability variation curves are shown in Figs. 12 and 13. In Fig. 12, the value of $k_m/k_0$ in the

influenced by the deformation of the formation and the pore structure. During the depletion-type exploitation of the formation, the deformation of the formation leads to the evolution of pores and natural fractures. Initially, stress changes during fracturing cause contraction or closure, temporarily decreasing permeability. Over time, the formation adapts and pore structure readjusts, increasing permeability. In which due to formation non-uniformity, the near-well zone is more susceptible to external influences with more natural fractures and pores. This causes delayed production impact away from the wellbore, shifting the minimum value outward. Matrix permeability is more sensitive to external pressure than natural fracture permeability, leading to an earlier shift of the minimum value towards the far-well zone.

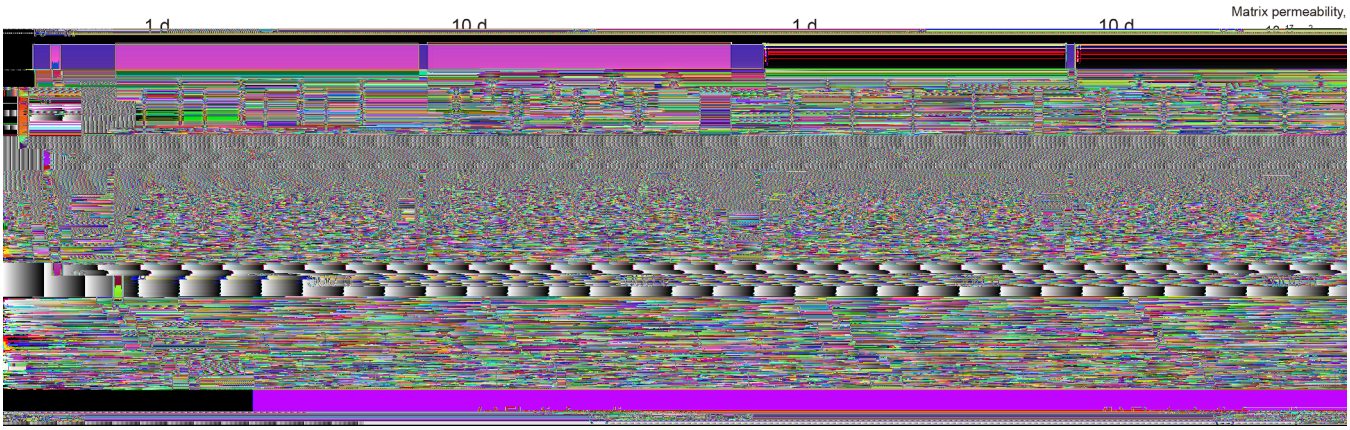


**Fig. 10.** Matrix permeability distribution at different times.

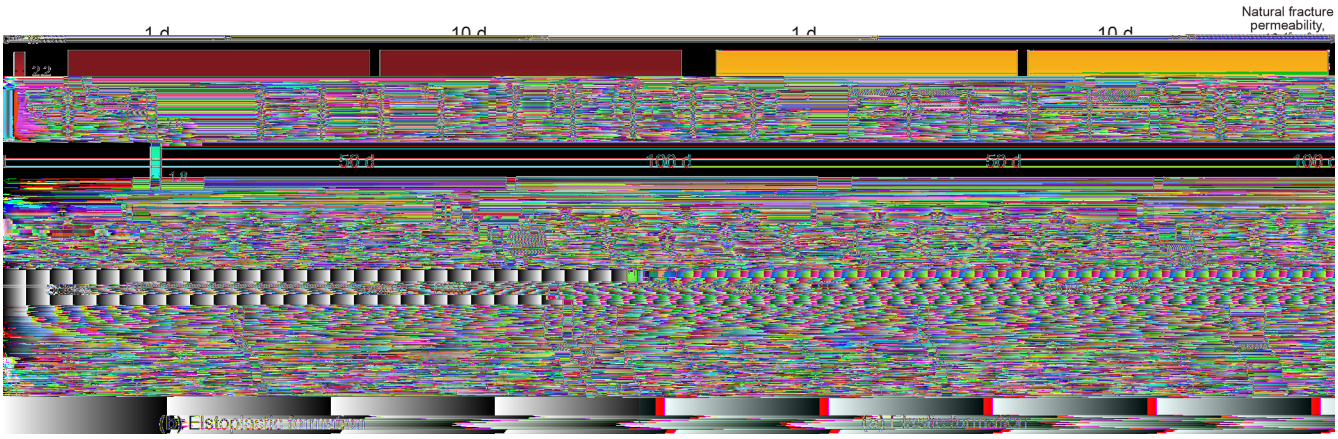


**Fig. 11.** Natural fracture permeability distribution at different times.

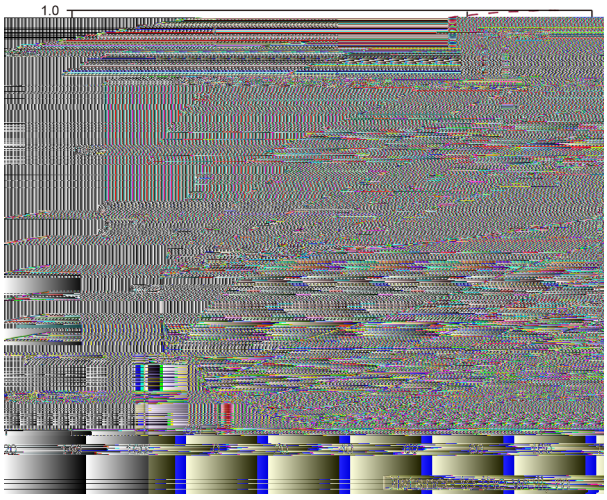


**Fig. 12.** Matrix permeability variations over time and distance.

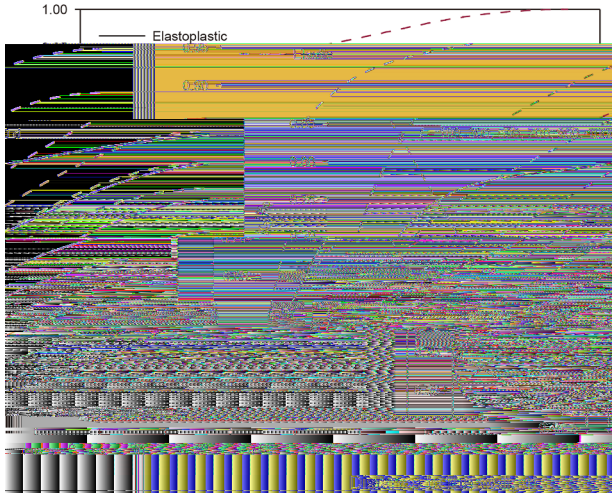


**Fig. 13.** Natural fracture permeability variations over time and distance.

### 4.3. Effect of elastoplastic deformation on production

The production rate and cumulative production variations of elastic and elastoplastic formations under different BHP is shown in Fig. 14. In Fig. 14(a), as the time increases in the elastic formation, the production rate decreases and the cumulative production increases. Both curves decline with increasing BHP. In Fig. 14(b), as the time increases in the elastoplastic formation, the daily production decreases and the cumulative production increases. However, both curves first rise and then fall with

increasing BHP. Cumulative production changes under BHP are shown in Fig. 15.

As shown in Fig. 15, the production of elastoplastic formations reaches its maximum around BHP of 31.5 MPa. Additionally, when the pressure is below 31.5 MPa, the production of elastic formations is higher than that of elastoplastic formations; while when the pressure exceeds 31.5 MPa, the production of elastic formations is lower than that of elastoplastic formations. Fig. 16 illustrates that, at a BHP of 25 MPa, the cumulative gas and water production in the elastic model exceed those in the elastoplastic model. The gas production is higher by 17.6%, and the water production is higher by 14.9%.

With constant original formation pressure, a decrease in flow pressure increases the production pressure differential, enhancing shale gas flow and recovery rate. In elastic formations, production increases as the flow pressure decreases. But in elastoplastic formation, higher pressure differentials cause plastic deformation, reducing pore channels and fluid movement,

**Fig. 17.** Matrix and natural fracture permeability variations over time and distance.

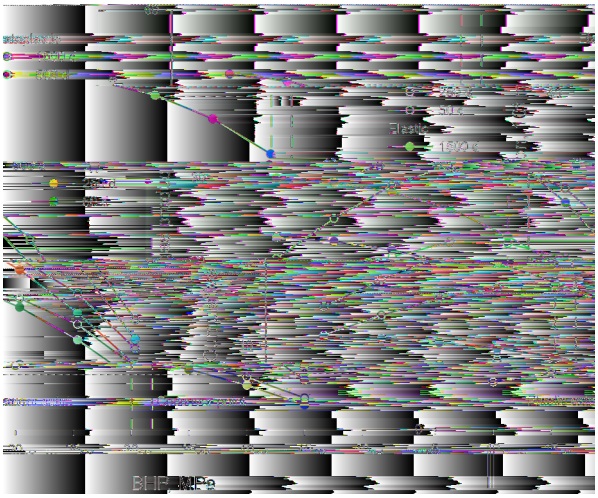

**Fig. 18.** Cumulative gas production of elastic and elastoplastic formations over time.

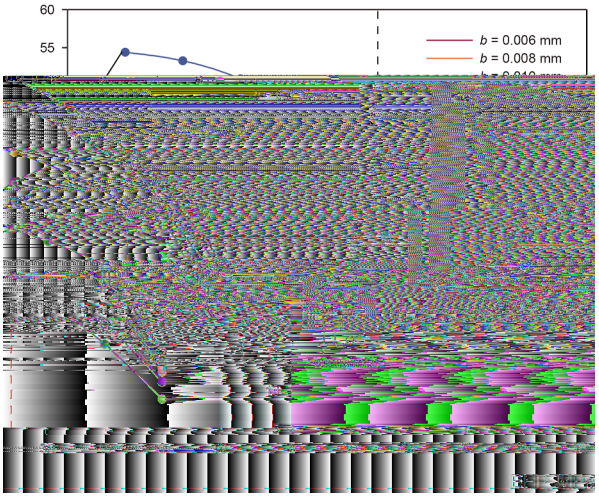


**Fig. 19.** Cumulative gas production under different natural fracture apertures.

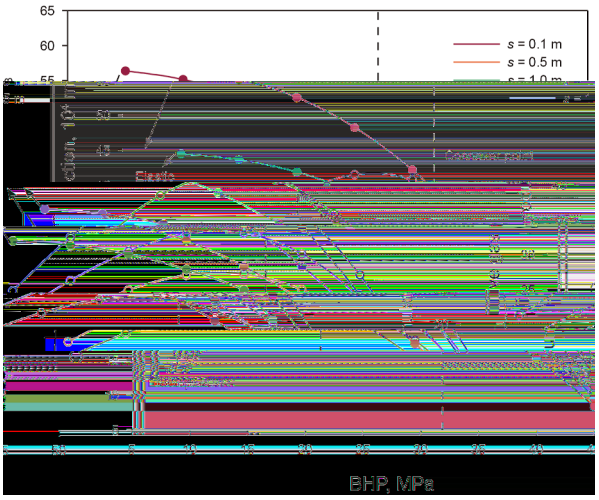


**Fig. 20.** Cumulative gas production under different natural fracture spacing.

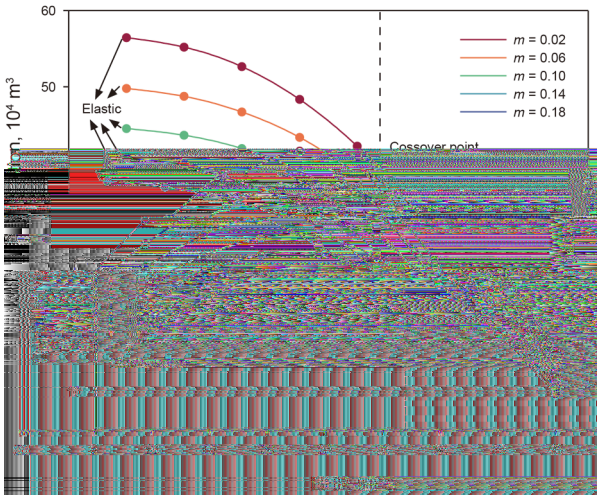


**Fig. 22.** Cumulative gas production under different stress sensitivity parameters.

### 4.4. Effect of model parameters on production

In this section, we examine the influence of various parameters on deep shale gas production. Each parameter is changed individually while others remain constant, as summarized in Table 3. The parameters examined include natural fracture aperture, natural fracture spacing, initial matrix permeability, stress sensitivity, Poisson's ratio, and original reservoir pressure.

#### 4.4.1. Natural fracture aperture

The cumulative production of elastic and elastoplastic formations is presented in Fig. 19 as a function of BHP under various natural fracture apertures. As the aperture increases from 0.006 to 0.012 mm, the rate of cumulative production growth slows in both models. The intersection point between elastic and elastoplastic production remains constant at 31.5 MPa. Maximum elastoplastic production occurs at 25 and 30 MPa. Overall, when BHP < 31.5 MPa, elastic formations yield 52.30% more production than elastoplastic ones. Therefore, for elastic formations, maintaining BHP below 31.5 MPa results in higher production. Conversely, when BHP > 31.5 MPa, elastoplastic formations yield 21.10% more production than elastic ones, indicating that after the formation undergoes elastoplastic deformation, BHP above 31.5 MPa leads to increased production.

#### 4.4.2. Natural fracture spacing

Fig. 20 shows the cumulative production over 1500 d versus BHP for different natural fracture spacing. As the spacing increases from 0.1 to 1.5 m, the production from both elastic and elastoplastic formations declines, but at a diminishing rate. The intersection point remains at 31.5 MPa, unaffected by natural fracture spacing. Peak elastoplastic production occurs at 25 and 30 MPa. When BHP < 31.5 MPa, elastic formations produce 52.88% more than elastoplastic ones. When BHP > 31.5 MPa, elastoplastic formations produce 22.21% more than elastic ones. This suggests that for elastic formations, BHP should be kept below 31.5 MPa for higher production, whereas after elastoplastic deformation, BHP above 31.5 MPa enhances production.

#### 4.4.3. Initial matrix permeability

Fig. 21 shows the cumulative production over 1500 d versus BHP for different initial matrix permeability. As the permeability increases, both elastic and elastoplastic production rise at an accelerating rate. The intersection point remains unchanged

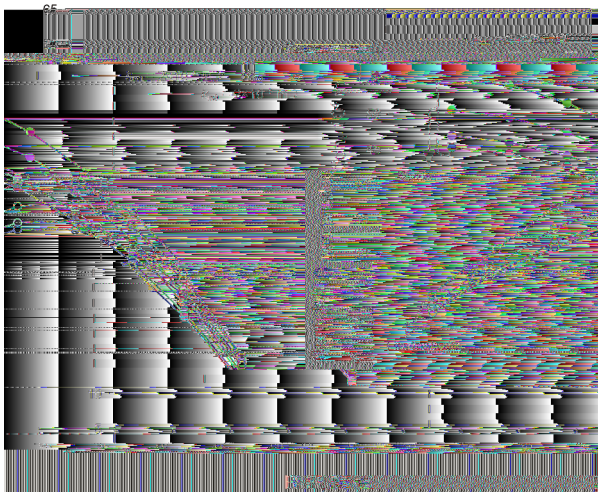

**Fig. 21.** Cumulative gas production under different initial matrix permeability.


**Fig. 23.** Cumulative gas production under different Poisson's ratios.

despite permeability variations. When BHP < 31.5 MPa, elastic formations yield about 53.96% more than elastoplastic ones. When BHP > 31.5 MPa, elastoplastic formations yield about 20.81% more than elastic ones. It indicates that maintaining BHP below 31.5 MPa optimizes production in elastic formations, while after elastoplastic deformation, BHP above 31.5 MPa yields higher production.

#### 4.4.4. Stress sensitivity parameter

Fig. 22 shows the cumulative production of elastic and elastoplastic formations versus BHP for different stress sensitivity parameters. As the stress sensitivity parameter increases from 0.02 to 0.18, the cumulative production decreases in both models. Peak elastoplastic production occurs at 25 and 30 MPa. When BHP < 31.5 MPa, elastic formations yield about 52.77% more than elastoplastic ones. When BHP > 31.5 MPa, elastoplastic formations yield about 21.14% more than elastic ones. For elastic formations, keeping BHP below 31.5 MPa maximizes production, while after elastoplastic deformation, exceeding 31.5 MPa enhances output.

#### 4.4.5. Poisson's ratio

Fig. 23 shows the cumulative production over 1500 d versus BHP for different values of Poisson's ratio. As Poisson's ratio increases from 0.10 to 0.25, the cumulative production decreases in both elastic and elastoplastic models. The intersection point shifts along the line $y = -161315.5x + 5509460.2$, showing Poisson's ratio affects its lateral movement. Maintaining elastoplastic reservoir BHP between 25 and 30 MPa leads to higher production. Below the line $y$, elastic formations yield 51.53% more than elastoplastic ones, above the line $y$, elastoplastic formations yield 21.75% more than elastic ones. For elastic formations, BHP

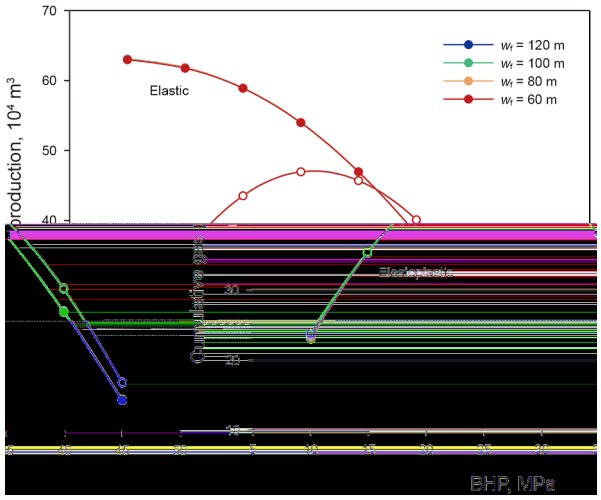


**Fig.**

When BHP < 31.5 MPa, the elastic formation exhibits approximately 64.32% higher production than the elastoplastic formation. Conversely, when BHP > 31.5 MPa, the elastoplastic formation yields about 14.94% higher production than the elastic formation. This indicates that maintaining BHP below 31.5 MPa enhances production in elastic formations, whereas keeping BHP above 31.5 MPa after elastoplastic deformation occurs leads to higher production.

#### 4.4.8. Hydraulic fracture half-length

Fig. 26 illustrates the variation in 1500-d cumulative production under different hydraulic fracture half-lengths. As the hydraulic fracture half-length increases, production decreases slightly in both elastic and elastoplastic formations, though the reduction is marginal and shows no significant variation. Notably, the intersection point remains constant despite changes in fracture half-length. When BHP < 31.5 MPa, the elastic formation demonstrates approximately 59.85% higher production than the elastoplastic formation. Conversely, when BHP > 31.5 MPa, the elastoplastic formation yields about 15.09% greater production than the elastic formation.

#### 4.4.9. Hydraulic fracture spacing

Fig. 27 demonstrates the variation of 1500-d cumulative production with BHP under different hydraulic fracture spacing. The results show that as the fracture spacing increases, production in both elastic and elastoplastic formations exhibits a slight upward trend, though the increment remains relatively minor with no significant variation. Remarkably, the intersection point maintains its position despite changes in fracture spacing. When BHP < 31.5 MPa, elastic formations outperform elastoplastic formations by approximately 63.36% in production. Conversely, when BHP > 31.5 MPa, elastoplastic formations show about 15.02% higher production than elastic formations.

### 4.5. Analysis of principal factors

The production of deep shale gas from fractured horizontal wells is influenced by various factors, with differing impacts on elastic and elastoplastic formations. To analyze the main factors, variables such as BHP, initial reservoir pressure, Poisson's ratio, initial matrix permeability, stress sensitivity, natural fracture spacing, and aperture are considered, using cumulative gas production over 1500 d to determine primary and secondary relationships, as shown in Fig. 28.

Results show that among all factors, initial reservoir pressure has the greatest impact on elastoplastic formation production, followed by natural fracture spacing. BHP has the greatest impact on elastic formation production, followed by initial reservoir pressure. Thus, the main factors affecting deep shale gas production are initial reservoir pressure, BHP, and natural fracture spacing.

## 5. Conclusions

This paper establishes a fully coupled model for hydraulic fracturing in deep shale gas reservoirs, considering post-fracturing elastoplastic deformation. It describes production performance with flow-geomechanics coupling. Through analysis, the following conclusions are drawn:

(1) The initial fracturing of the formation leads to a temporary contraction, resulting in a decrease in permeability. However, subsequent pore structure readjustment during production causes an increase in permeability. Formation heterogeneity leads to varied production responses across regions, with areas distant from the well responding more slowly, causing the minimum permeability to shift right over time.

(2) As the bottom-hole pressure (BHP) increases, the elastic production decreases, while elastoplastic production initially increases and then decreases. The temporal aspect of production does not exert an influence on the position of the elastoplastic maximum point or the intersection point between elastic and elastoplastic production.

(3) When the initial reservoir pressure is 50 MPa and the BHP is less than 31.5 MPa, elastic exploitation is preferable; when the BHP exceeds 31.5 MPa, elastoplastic exploitation is preferable.

(4) Poisson's ratio and original formation pressure mainly affect the elastic and elastoplastic intersection point. The initial reservoir pressure determines the optimal range of BHP for elastoplastic formations, ideally 0.5 to 0.625 times the original formation pressure for higher production.

(5) Among the influencing factors, initial reservoir pressure has the greatest impact on elastoplastic formation production, followed by natural fracture spacing. BHP has the greatest influence on elastic formation production, followed by original formation pressure.

**CRediT authorship contribution statement**

**Dong-Yan Fan:** Writing – review & editing, Supervision, Resources, Funding acquisition. **Can Yang:** Writing – review & editing, Writing – original draft, Visualization, Validation, Investigation. **Hai Sun:** Supervision, Project administration, Funding acquisition. **Jun Yao:** Supervision, Methodology, Funding acquisition. **Xia Yan:** Supervision, Software, Resources. **Lei Zhang:** Methodology, Funding acquisition, Conceptualization. **Cun-Qi Jia:** Supervision, Funding acquisition. **Gloire Imani:** Project administration. **Si-Cen Lai:** Formal analysis.

Xu, F.S., Wang, F.P., Zhang, J.T., et al., 2021. Development strategy for the scale and efficiency of deep shale gas in China. Journal of Natural Gas Industry 41 (1), 205–213. https://doi.org/10.3787/j.issn.1000-0976.2021.01.019 (in Chinese).

Xu, P., Yu, B., 2008. Developing a new form of permeability and Kozeny–Carman constant for homogeneous porous media by means of fractal geometry. Adv. Water Resour. 31, 74–81. https://doi.org/10.1016/j.advwatres.2007.06.003.

Yao, J., Huang, C., Liu, W., et al., 2018. Key mechanical issues in deep oil and gas reservoir development. Sci. China Phys. Mech. Astron. 48, 044701. https://doi.org/10.1360/SSPMA2017-00286 (in Chinese).

Yi, D., Yang, Z., Yi, L., et al., 2025. Simulation of dynamic pulse fracturing in elastoplastic media based on a mixed-mode fatigue phase-field model. Comput. Geotech. 179, 107043. https://doi.org/10.1016/j.compgeo.2024.107043.

Yu, R.Z., Wang, C.H., Zhang, X.W., Hu, Z.M., Sun, Y.P., Guo, W., Duan, X.G., Wang, M. Z., 2022. Development characteristics and enlightenment of Eagle Ford deep shale gas reservoirs in North America. Coal Geol. Explor. 50 (9), 32–41. https://doi.org/10.12363/issn.1001-1986.21.12.0815 (in Chinese).

Zeng, Q., Yao, J., Shao, J., 2019. Effect of plastic deformation on hydraulic fracturing with extended element method. Acta Geotech 14, 2083–2101. https://doi.org/10.1007/s11440-018-0748-0.

Zhang, H., 2020. Study on Plastic Zone of Vertical Wellbore. Master's Thesis. Xi'an Shiyou University. https://link.cnki.net/doi/10.27400/d.cnki.gxasc.2020.000156 (in Chinese).

Zhang, H., Liu, J., Elsworth, D., 2008. How sorption-induced matrix deformation affects gas flow in coal seams: A new FE model. Int. J. Rock Mech. Min. Sci. 45, 1226–1236. https://doi.org/10.1016/j.ijrmms.2007.11.007.

Zhang, W., Wang, Q., Ning, Z., Zhang, R., Huang, L., Cheng, Z., 2018. Relationship between the stress sensitivity and pore structure of shale. J. Nat. Gas Sci. Eng. 59, 440–451. https://doi.org/10.1016/j.jngse.2018.09.010.

Zhao, K., Li, R., Feng, Y., et al., 2022. Distribution of plastic zone around horizontal wells in hydrate reservoir in nonuniform in-situ stress field. J. Cent. S. Univ. 53 (3), 952–962. https://doi.org/10.11817/j.issn.1672-7207.2022.03.017 (in Chinese).

Zhao, Y., Lu, G., Zhang, L., Wei, Y., Guo, J., Chang, C., 2020. Numerical simulation of shale gas reservoirs considering discrete fracture network using a coupled multiple transport mechanism and geomechanics model. J. Petrol. Sci. Eng. 195, 107588. https://doi.org/10.1016/j.petrol.2020.107588.

Zhu, W., Chen, Z., Liu, K., 2022. A new meshless method to solve the two-phase thermo-hydro-mechanical multi-physical field coupling problems in shale reservoirs. J. Nat. Gas Sci. Eng. 105, 104683. https://doi.org/10.1016/j.jngse.2022.104683.

Zhu, W., Chen, Z., He, X., Tian, Z., Wang, M., 2023. Numerical investigation of influential factors in hydraulic fracturing processes using coupled discrete element-lattice Boltzmann method. J. Geophys. Res. Solid Earth 128, e2023JB027292. https://doi.org/10.1029/2023JB027292.